Published in final edited form as:

Nat Nanotechnol. 2010 June ; 5(6): 465–472. doi:10.1038/nnano.2010.58.

Tuning Payload Delivery in Tumour Cylindroids using Gold Nanoparticles

Byoungjin Kim[1], **Gang Han**[2], **Bhushan Toley**[1], **Chae-kyu Kim**[2], **Vincent M. Rotello**[2], and **Neil S. Forbes**[1]

[1] Department of Chemical Engineering, University of Massachusetts, Amherst, Amherst, MA 01003-9303

[2] Department of Chemistry, University of Massachusetts, Amherst, Amherst, MA 01003-9303

Abstract

Nanoparticles have great potential as controllable drug delivery vehicles because of their size and modular functionality. Timing and location are important parameters when optimizing nanoparticles for delivery of chemotherapeutics. Here we show that positively- and negatively-charged gold nanoparticles carrying either fluorescein or doxorubicin molecules move and localize differently in an in vitro three dimensional model of tumour tissue. Fluorescence microcopy and mathematical modelling showed that uptake, and not diffusion, is the dominant mechanism in particle delivery. Our results suggest that positive particles may be more effective for drug delivery because they are more significantly taken up by proliferating cells. Negative particles, which diffused faster, may perform better when delivering drugs deep into the tissues. An understanding of how surface charge can control tissue penetration and drug release may overcome some of the current limitations in drug delivery.

Keywords

gold nanoparticles; surface charge; tumour cylindroids; cellular uptake; tissue penetration; drug delivery

Inefficient delivery limits the efficacy of many chemotherapeutic treatments[1–5]. Overcoming delivery limitations requires precise control of interstitial diffusion and cellular

Correspondence to Neil S. Forbes, Department of Chemical Engineering, University of Massachusetts, Amherst, 159 Goessmann Laboratory, 686 North Pleasant Street, Amherst, MA 01003-9303, Phone: (413) 577-0132, Fax: (413) 545-1647, forbes@ecs.umass.edu.

Author Contributions

N.F. and V.R. conceived and designed the experiments. B.K., G.H., B.T. and C.K. performed the experiments: G.H. synthesized the FITC nanoparticles; C.K. synthesized the DOX nanoparticles; B.K. performed all cell and cylindroid experiments with FITC nanoparticles and wrote all mathematical models; and B.T. performed all cylindroid and cell experiments with DOX nanoparticles. B.K., B.T. and N.F. analyzed the data. V.R. contributed materials. B.K. and N.F. co-wrote the paper. All authors discussed the results and commented on the manuscript.

Additional information

Supplementary information accompanies this paper at www.nature.com/naturenanotechnology. Reprints and permission information is available online at http://npg.nature.com/reprintsandpermissions/.

uptake. Tumours typically have irregularly formed vasculature with large intervessel distances and heterogeneous populations of cells[6]. These populations are often unresponsive to standard therapy because of their distance from blood vessels and resistance to molecular uptake[3,7]. This limited efficacy prevents complete cell clearance per drug cycle, which can eventually lead to tumour regrowth, metastatic disease, and poor treatment outcomes[1–3,8–9].

Colloidal gold nanoparticles have great potential to overcome delivery limitations because of their biocompatibility, low toxicity, small size, and tunable surface functionalities[10–11]. Functionality can be tuned by modifying the composition of functional molecules in the mixed monolayer on the surface of gold nanoparticles[12–14]. In cancer cell cultures, surface properties have been shown to regulate cellular uptake, intracellular release, and distribution in subcellular compartments[15–18]. Modification of the surface properties of gold nanoparticles therefore has the potential to control accumulation in tumours, and where drug payloads are released.

Three-dimensional *in vitro* tumour models provide an important tool for the optimization of efficient intratumoural drug delivery. Multicellular tumour cylindroids provide a unique platform to systematically monitor extracellular diffusion, cellular uptake, and molecular release from nanoparticles in real time (Figure 1a). Tumour cylindroids are spheroids constrained between two parallel surfaces[19–20]. The geometry of cylindroids allows only radial diffusion from the peripheral edge to the center, simplifying analysis. Through the optically accessible cross section, the local concentrations of nanoparticles and dyes can be measured with standard fluorescence microscopy. Importantly, cylindroids consist of heterogeneous cell populations that arrange depending on the distance from the peripheral edge: cells in the periphery are mostly proliferating and cells in the center are mostly apoptotic and necrotic[19–24]. This radial organization mimics the distribution of cells around blood vessels in tumours *in vivo* (Figure 1b)[24–25].

We hypothesized that different surface charges can control the penetration of nanoparticles and the location of cellular uptake and release. Thioalkylated fluorescein-labeled gold nanoparticles (2 nm core diameter, 6 nm overall with ligand) with positive and negative surface charges were synthesized (Figure 1c) and administered to cylindroids. Fluorophore concentrations were measured as functions of time and radial position. The diffusion of gold nanoparticles in extracellular matrix (Matrigel) was measured in a linear cell-free chamber. A mathematical model was developed to discriminate between fluorescence from particles and released fluorescein, and to calculate the rates of cellular uptake/release (Figure 1d) as a function of position in cylindroids. Determined parameters were used to predict the dynamics of particle transport and release from blood vessels in a conceptualized tumour (Figure 1b). Positive and negative gold nanoparticles conjugated with doxorubicin (DOX) were similarly synthesized, and our results show that surface charge can be used to control tissue penetration and drug release.

Uptake of fluorescent gold nanoparticles

Gold nanoparticles were synthesized with gold cores protected by mixed monolayers[14,26] to provide tunable probes for delivery. The monolayers on these particles consisted of

thioalkylated fluorescein isothiocyanate (**FITC-SH**) and either thioalkyl tetra (ethylene glycol)lyated trimethyl ammonium or thioalkyl tetra (ethylene glycol) lyated carboxylic acid to create cationic (**p-FITC-AuNP**) and anionic (**n-FITC-AuNP**) gold nanoparticles (Figure 1c), respectively[27]. The surface zeta potentials of **p-FITC-AuNP** and **n-FITC-AuNP** were measured to be +30 and −36mV, respectively.

The fluorescence intensities of **p-FITC-AuNP**, **n-FITC-AuNP** and free fluorophore (**FITC-SH**) were used to calibrate fluorescence intensity and determine the **FITC-SH** loading ratio on each gold core. Fluorescence intensities were linearly proportional to concentration (Figure 2a). Conjugation to gold cores quenches FITC-SH fluorescence. Treatment with potassium cyanide to recover quenched fluorescence increased the intensities of the **p-FITC-AuNP** and **n-FITC-AuNP** solutions by 4 and 2.4 times, respectively (Figure 2a). The ratio of released ligand to free ligand fluorescence indicates that the loading ratios were 7.5 and 8.3 for **p-FITC-AuNP** and **n-FITC-AuNP**, respectively. The linear relationship between intensity and concentration indicates that self-quenching did not have a large effect over this concentration range.

In monolayer cell culture, all **FITC-SH** release from nanoparticle cores was intracellular (Figure 2b–c). Intracellular release of **FITC-SH** is mediated by cytoplasmic thiol compounds, of which reduced glutathione (GSH) is the most abundant[28]. Similar selectivity would be observed *in vivo*, because the intracellular concentration of glutathione (1~10mM) is considerably higher than in the plasma (~2μM)[29–30]. After removal of media containing **FITC-AuNP**, stronger green fluorescence was observed across the cells treated with **p-FITC-AuNP** (Figure 2b) compared to **n-FITC-AuNP** (Figure 2c). This observation indicates that cellular uptake and dissociation were greater for cationic gold nanoparticles, potentially mediated by interactions of the particles with serum proteins.

Cellular uptake and release in cylindroids was dependent on particle surface charge and radial position (Figure 3). Intra- and extracellular fluorescence was measured in cylindroids in real time using fluorescence microscopy (Figure 3a, c, e). A clear morphological boundary could be seen between the inner and outer regions of cylindroids (Figure 3a, c, e), which have been shown to contain viable and apoptotic microenvironments, respectively[19–20,24]. In the outer region, cationic particles produced more fluorescence than free FITC and anionic particles (Figure 3a–f). For positive particles, the fluorescence intensity in the outer region increased with time and eventually the entire cylindroid became fluorescent (Figure 3a, b). For negative particles, the fluorescence intensity in the outer region did not increase (Figure 3c) and remained unchanged after 11hrs (Figure 3d). This preferential uptake of cationic gold nanoparticles by proliferating cells was similar to the difference observed in the monolayer cultures (Figure 2a–c). In the inner region, fluorescence appeared at earlier time points than in the outer region and appeared regardless of surface charge (Figure 3a–d). Images acquired at 4 and 8hrs (See Supplementary Information) were spatially similar but fainter than those at 11hrs. In cylindroids incubated with free FITC, strong fluorescence appeared only in the inner region (Figure 3e) and the intensity profiles remained unchanged for 11 hrs after treatment (Figure 3f). The enhanced cellular uptake of positive particles by proliferating cells may be caused by electrostatic interaction with the net negative surface

charge of the plasma membrane[31–32], which has also be observed in liposomal and polymeric delivery systems[33–35].

Particle charge had a pronounced effect on the dynamics of particle uptake and fluorophore release (Figure 3g–h). These dynamics where observed by averaging the behavior in the inner and outer regions, which were defined as annuli 175–200μm from the center and 25–50μm from the periphery of three cylindroids (hashed bars in Figure 3b, d). In cylindroids treated with positive particles, fluorescence intensities increased monotonically (Figure 3g). The behavior was considerably different for cylindroids treated with negative particles, in which the fluorescence intensity saturated with time and eventually reached a plateau (Figure 3h). Comparing inner and outer regions, the time-dependent behavior of cellular uptake/release was functionally similar for both particle types (Figure 3g, h).

Two possible causes for the early appearance of fluorescence at the center of cylindroids following nanoparticle administration (Figure 3a–d) are: (1) an increased rate of uptake by apoptotic/necrotic cells or (2) an increased rate of fluorophore dissociation due to higher thiol concentrations. The dye *o*-phthaldialdehyde (OPA) reacts non-enzymatically with amino acids and their derivatives in the presence of thiol compounds, a technique that has been widely used to measure intracellular glutathione concentration[36–37]. Staining with OPA showed that the concentration of thiol compounds was higher in the outer region and decreased toward the center of the cylindroids (Figure 3i). This location of cellular thiol compounds was opposite to the pattern of fluorescence from nanoparticles (Figure 3a–d). We have previously shown that centers of cylindroids are composed of apoptotic and necrotic cells[19–20,24], and these cells preferentially take up particles compared to viable cells (Figure S2a–c) because they have lost membrane integrity[19–20]. Together, these observations demonstrate that cellular uptake is the dominant mechanism. If dissociation, and not uptake, were the limiting mechanism then fluorescence from released fluorophore would have been greater in periphery than the center.

Ligand dissociation was expected to be entirely intracellular because of higher levels of glutathione relative to the extracellular environment. Confocal microscopy was used to verify that extracellular dissociation did not occur (Figure 3j). Following incubation with nanoparticles for 36hrs, **FITC-SH** release was observed primarily inside cells (Figure 3j). Intracellular localization of dissociation was consistent across the diameter of cylindroids: fluorescence was observed only inside cells in both the inner and outer regions. In addition, observed fluorescence patterns were conserved in the z-direction (away from the objective) supporting the use of epifluorescent microscopy for quantitative penetration measurements.

Uptake of doxorubicin nanoparticles

To further probe the potential therapeutic applications of engineered nanoparticles, we fabricated particles featuring a doxorubicin prodrug tethered through an acid-labile hydrazone linkage to a thiol ligand (Figure 1c). Similar to FITC-AuNP, a positive surface charge dramatically enhanced uptake of DOX-AuNP into proliferating peripheral cells compared to negative particles and free drug (Figure 4). In cylindroids positive particles delivered more doxorubicin than negative particles (Figure 4a–b). By location, positive

particles delivered significantly more doxorubicin to viable cells in the cylindroid periphery, compared to negative particles and free drug which were preferentially taken up by dead cells at the cylindroid center ($P<0.05$; Figure 4d). This charge dependent localization was consistent over the 46 hours of the experiment ($P<0.05$; Figure 4e), during which the concentration of particles and free drug increased within cylindroids (Figure 4a–c, radial profiles). The similarity of these results with the FITC results (Figure 3) supports the prediction that nanoparticles with positive surface charges will outperform negative particles for most applications and confirms that charged gold nanoparticles have the potential to overcome drug penetration barriers and deliver clinically relevant anti-cancer drugs.

Diffusion of nanoparticles in matrix material

In addition to regulating cellular uptake, surface charge also significantly affected the diffusivity of gold nanoparticles in the extracellular matrix. Diffusivity in the extracellular matrix was modeled using a cell-free diffusion chamber, which confined Matrigel between a trench cut in a polycarbonate block and the bottom surface of well plate (Figure 5a). In this model, diffusion occurred in only one direction: from the exposed surface to the center of the trench. Concentrations of FITC and FITC-AuNP were measured as a function of time and location by acquiring a series of fluorescence images along the longitudinal direction every 2hrs.

Intensity gradients decreased from the edge toward the center of the Matrigel trench, and the slope of the gradients diminished with time (Figure 5b, c). Diffusion coefficients were determined by non-linear least square fitting of the intensity gradients to a Fickian diffusion model (Figure 5c). The diffusion coefficient for FITC was $42 \pm 2 \times 10^{-7}$ cm^2/s, which was larger than both gold nanoparticles by an order of magnitude (Figure 5d). Simulations with this diffusion coefficient matched concentration profiles seen in cylindroids (Figure 3), suggesting that diffusion alone controlled the delivery of free FITC. Anionic gold nanoparticles had a larger diffusion coefficient, $9.0 \pm 0.1 \times 10^{-7}$ cm^2/s, than cationic nanoparticles, $7.6 \pm 0.1 \times 10^{-7}$ cm^2/s ($P<0.005$; n=3; Figure 5d).

The decreased diffusion coefficient of positive particles suggests that electrostatic interactions with negatively charged macromolecules in the matrix slowed particle diffusion. The major components of extracellular matrix in tumours and spheroids are collagen and proteoglycans[38–40]. Matrigel is derived from tumour matrix materials[41], which are negatively charged under physiological conditions[31]. Because cationic and anionic particles have similar molecular weights and hydrodynamic radii, it is likely that electrostatic interactions with the matrix are the primary cause of the difference between diffusion coefficients.

Three mechanisms control the timing and location of drug delivery into tumours using nanoparticles: diffusion, cellular uptake, and ligand dissociation. Our results suggest that of these three, cellular uptake is the dominant mechanism. In all cylindroids, fluorescence appeared early in the center of cylindroids (Figure 3). If diffusion were the limiting mechanism, fluorescence would first appear at the outside edge and progress into the center.

The measured diffusion coefficients in matrix material (Figure 5d) confirm that diffusion can account for the rapid appearance of particles in cylindroid centers.

Modelling diffusion and cellular uptake/release

A descriptive mathematical model was developed to interpret the coupled effects of extracellular diffusion (Figure 1b) and cellular uptake/release (Figure 1d) on molecular nanoparticle delivery. The model framework was designed to show how dynamic nanoparticle measurements in cylindroids provide preliminary information about nanoparticle behavior under physiological conditions. The model consisted of two transient partial differential equations, one for gold nanoparticles, and the other for free intracellular fluorophore. Concentration profiles of particles and released ligand were predicted using *in vitro* calibrations of ligand release (Figure 2a). Based on confocal microscopy results (Figure 3j), all ligand dissociation was modeled as an intracellular reaction. Internalization of FITC-AuNPs and release of **FITC-SH** were modeled as a single reaction with radially dependent forward, k_1, and reverse rate constants, k_2 (Figure 1d and Figure S2 in supplemental material). Nanoparticle diffusion coefficients were derived from measured diffusivities in Matrigel (Figure 5).

The modelling results fit well to the experimental data and predict that positively charged particles will outperform negative particles for most but not all applications (Figure 6). The modelling results (solid lines in Figure 6a–b) captured a number of key characteristics of the fluorescent patterns shown in Figure 3 and the experimental data points in Figure 6a–b. First, a higher fluorescence was seen in the inner regions than the outer at early time points. Second, positive particles showed a monotonic increase in fluorescence, and this increase was more pronounced in the outer regions. Third, negative particles displayed saturation of fluorescence. By separating the fluorescence contributions from free and bound fluorophore, the modelling results indicate that particle diffusion was rapid and the appearance of free fluorophore by uptake and dissociation controlled overall fluorescence (Figure 6c). Calculated kinetic rates suggest that viable cells had a higher net uptake of positive particles because of a lower export rate, k_2, in both inner and outer regions ($P<0.05$; $n=3$; Figure 6d). For negative particles, the forward rate constant was only larger in the inner region ($P<0.05$; $n=3$; Figure 6d).

Modelling predictions were based on a hypothetical tumour whose geometry was inverted: particles diffused from a blood vessel ($0<r<5\mu m$) into tumour tissue ($r>5\mu m$). Because of their greater diffusion coefficient, negative particles penetrated deeper into the interstitium at all times (Figure 6e). However, the concentration of released intracellular ligand was greater for positive particles, because of their larger net uptake rate (Figure 6f). This predicted deep penetration of negative particles may be mitigated by elevated interstitial fluid pressures often seen in tumours *in vivo*[42–44]. For both particles, the concentration of released ligand reached a maximum between 20 and 30 hours (Figure 6f). Regions of proliferating (10–70μm) and quiescent (75–120μm) cells were defined based on single cell analysis performed in cylindroids[24]. The average concentrations of released ligand for positive particles in the proliferating and quiescent regions were more than 11-fold and 8-fold greater at all times, respectively (Figure 6g). Deep in the tissue (>1mm) the

concentration of released ligand was greater for negative particles at later times (>20hr; Figure 6h). These results suggest that positive particles will release more ligand to most cells at all times (Figure 6f and g) and therefore be advantageous for most applications. Complementarily, negative particles would have an advantage delivering drugs deep into tissue (Figures 5d and 6h) and would be useful treating tumours with large inter-vessel spacing and high hypoxic tolerance.

Conclusions

Using a combination of experimental in vitro tumour models and mathematical modelling, we showed that under most circumstances, positively charged nanoparticles improved delivery of payloads to the majority of cells in tumours, whereas negatively charged particles would perform better when delivering drugs deep into tissues. Positive particles had significantly higher uptake and dissociation by viable cells, whereas negative particles diffused faster. Both positive and negative particles penetrated tissues rapidly and for both, the rate of cellular uptake and dissociation was slower than extracellular diffusion. The mathematical models suggested that the rate of cellular uptake of both particles was fast in apoptotic and necrotic tissues, and the uptake kinetics of positive particles was irreversible, whereas it is reversible for negative particles over the time scales investigated. The ability to tune surface charge to control tissue penetration and drug release makes gold nanoparticles a flexible and powerful drug delivery vehicle.

Experiments and methods

Synthesis and characterization of mixed monolayer-protected gold nanoparticles

Pentanethiol coated gold nanoparticles were synthesized according to the method reported by You *et. al.*[45] and as described in Supplementary Information. Zeta potentials were measured in triplicate by a MALVERN Zetasizer Nano ZS for 0.8μM nanoparticles in PBS buffer (pH=7.8, 20mM potassium phosphate, 100mM sodium chloride). Fluorescence intensities of p-FITC-AuNP, n-FITC-AuNP and FITC-SH were measured at 0.5 and 1.0μM in DMEM by fluorimetry (SPECTRAmax GEMINI XS, Molecular Devices) to calibrate fluorescence intensity and determine the FITC-SH loading ratios.

FITC-AuNP and Dox-AuNP uptake and ligand release in monolayer culture

LS174T human colon carcinoma cells were grown in Dulbecco's Modified Eagle's Medium (DMEM, 1g/L glucose) supplemented with 10% fetal bovine serum at 37°C with 5% CO_2 in a humidified incubator. Cells in monolayer cultures were incubated with 1μM FITC-AuNPs for 6hrs, and were washed with PBS three times before image acquisition. Confocal fluorescence microscope images were acquired with a Zeiss LSM510 microscope equipped with a 25x objective lens. A 488nm argon laser was used for excitation and emission was acquired at 505 nm (long pass).

FITC-AuNPs and Dox-AuNPs in cylindroids

Cylindroids were prepared from spheroids as described previously[19–20] and in Supplementary Information. After equilibration, cylindroids were treated with 125 μM

FITC, 1μM FITC-AuNP, 1 μM Dox, or 1 μM Dox-AuNP. Transmitted and fluorescence images were acquired with an Olympus IX71 microscope with a 10X objective at 0, 11, 21, 38, 46hrs after treatment. Radial fluorescence intensity profiles in cylindroids were generated using a customized script in ImageJ (NIH Research Services Branch). Average fluorescence intensities were determined for two annular regions: 175–200μm from the center (inner) and 25–50μm from the periphery (outer). For confocal fluorescence microscopy, cylindroids were prepared in 35mm glass bottom culture dishes. Images were acquired with a Zeiss LSM510 microscope equipped with a 63X oil-immersion objective. A 488nm argon laser was used for excitation and emission was acquired at 505 nm.

Thiol compounds in cylindroids

The distribution of GSH was determined by measuring the fluorescence intensity of *o*-phthaldialdehyde (OPA) derivatives. OPA reacts with amino acids in the presence of thiol compounds forming fluorescent derivatives[36–37]. Cylindroids were incubated with 250μl of 100μM OPA in PBS. Transmitted and fluorescence images were acquired 4, 18 and 36hrs after treatment. Samples were excited at 350 nm and measured at 460 nm.

Extracellular diffusion of FITC-AuNP

Diffusion of gold nanoparticles was measured in Matrigel in a loading module (Figure 5a) as described in Supplementary Information. The loading module was prepared by making a channel (3.1 × 0.5 × 6.2 mm; W × H × L) in the top of a polycarbonate block (9.6 × 4.8 × 6.2 mm). Before loading, the well plate was plasma treated for 5 min and sterilized with UV for 4hrs. The module was loaded with 12μl Matrigel, which was allowed to gelate at 37°C for 5min. Pre-warmed DMEM (2.0ml) was added to each well and after 2hrs, was replaced with DMEM containing 1μM FITC-AuNP. Transmitted and green fluorescence images were acquired every 2hrs for 36hrs. Spatial concentration profiles were obtained by averaging pixel values across the width of the channel. Diffusion coefficients of FITC, p-FITC-AuNP and n-FITC-AuNP were determined by fitting measured fluorescence intensities to a mathematical diffusion model. Numerical solutions were calculated using finite elements, and best-fit diffusion coefficients were determined by nonlinear least squares optimization in Matlab (MathWorks, Natick, MA).

Mathematical modelling of particle diffusion and cellular uptake in cylindroids

Internalization of gold nanoparticles from extracellular space and glutathione-mediated replacement were represented with a one-step reversible reaction

$$FITC - AuNP \underset{k_2}{\overset{k_1}{\rightleftharpoons}} FITC - SH + AuNP$$

where k_1 and k_2 are forward and reverse reaction constants. Coupled conservation equations for FITC-AuNPs and released FITC-SH incorporated expressions for extracellular nanoparticle diffusion and the kinetics of particle uptake and ligand release.

$$\frac{\partial C_{Particle}}{\partial t} = \frac{D_{eff}}{r} \cdot \frac{\partial}{\partial r}\left(r \frac{\partial C_{Particle}}{\partial r}\right) - f_v\left(k_1 C_{Particle} - k_2 C_{Ligand}\right) \quad (1)$$

$$\frac{\partial C_{Ligand}}{\partial t} = k_1 C_{Particle} - k_2 C_{Ligand} \quad (2)$$

From confocal measurements, the cell volume fraction, f_v, was found to be 0.48. The effective nanoparticle diffusion coefficients, D_{eff}, were derived from the Matrigel experiments. Reaction rates were assumed to be functions of position as described in the Supplementary Information. This model was solved using finite elements and fit to measured fluorescence concentrations by nonlinear least squares optimization in Matlab. Calculated fluorescence values were determined from the sum of the volume-fraction-weighted particle (FITC-AuNP) and released ligand (FITC-SH) concentrations. Calculated rate constants were reported as average values inside the inflection point, $r < R_t$ (inner) and between the inflection point and the edge, $R_t < r < 1$ (outer). Significance was determined using unpaired Student's t-tests with unequal variance. Particle diffusion and ligand released was modelled in a hypothetical tumour as described in Supplementary Information. In this model the blood was assumed to be well mixed and particles were cleared with a three hour half-life[46].

Supplementary Material

Refer to Web version on PubMed Central for supplementary material.

Acknowledgments

We gratefully acknowledge financial support from the National Institutes of Health (Grant Nos. 1R21CA112335-01A and 1R01CA120825-01A1) and the National Science Foundation (Grant No. DMI-0531171).

References

1. Hicks KO, Pruijn FB, Sturman JR, Denny WA, Wilson WR. Multicellular resistance to tirapazamine is due to restricted extravascular transport: A pharmacokinetic/pharmacodynamic study in HT29 multicellular layer cultures. Cancer Res. 2003; 63:5970–5977. [PubMed: 14522924]
2. Lankelma J, et al. Doxorubicin gradients in human breast cancer. Clin Cancer Res. 1999; 5:1703–1707. [PubMed: 10430072]
3. Minchinton AI, Tannock IF. Drug penetration in solid tumours. Nat Rev Cancer. 2006; 6:583–592. [PubMed: 16862189]
4. Jain RK. Transport of molecules, particles, and cells in solid tumors. Annu Rev Biomed Eng. 1999; 1:241–263. [PubMed: 11701489]
5. Primeau AJ, Rendon A, Hedley D, Lilge L, Tannock IF. The distribution of the anticancer drug doxorubicin in relation to blood vessels in solid tumors. Clin Cancer Res. 2005; 11:8782–8788. [PubMed: 16361566]
6. Vaupel P, Kallinowski F, Okunieff P. Blood flow, oxygen and nutrient supply, and metabolic microenvironment of human tumors: a review. Cancer Res. 1989; 49:6449–6465. [PubMed: 2684393]
7. Tredan O, Galmarini CM, Patel K, Tannock IF. Drug resistance and the solid tumor microenvironment. J Natl Cancer Inst. 2007; 99:1441–1454. [PubMed: 17895480]

8. Grantab R, Sivananthan S, Tannock IF. The penetration of anticancer drugs through tumor tissue as a function of cellular adhesion and packing density of tumor cells. Cancer Res. 2006; 66:1033–1039. [PubMed: 16424039]
9. Goldacre RJ, Sylven B. On the Access of Blood-Borne Dyes to Various Tumour Regions. Br J Cancer. 1962; 16:306–322. [PubMed: 13899681]
10. You CC, Verma A, Rotello VM. Engineering the nanoparticle-biomacromolecule interface. Soft Matter. 2006; 2:190–204.10.1039/b517354j
11. You CC, De M, Han G, Rotello VM. Tunable inhibition and denaturation of alpha-chymotrypsin with amino acid-functionalized gold nanoparticles. J Am Chem Soc. 2005; 127:12873–12881. [PubMed: 16159281]
12. Goodman CM, et al. DNA-binding by functionalized gold nanoparticles: mechanism and structural requirements. Chem Biol Drug Des. 2006; 67:297–304. [PubMed: 16629827]
13. McIntosh CM, et al. Inhibition of DNA transcription using cationic mixed monolayer protected gold clusters. J Am Chem Soc. 2001; 123:7626–7629. [PubMed: 11480984]
14. You CC, De M, Han G, Rotello VM. Tunable inhibition and denaturation of alpha-chymotrypsin with amino acid-functionalized gold nanoparticles. J Am Chem Soc. 2005; 127:12873–12881. [PubMed: 16159281]
15. Thomas M, Klibanov AM. Conjugation to gold nanoparticles enhances polyethylenimine's transfer of plasmid DNA into mammalian cells. Proc Natl Acad Sci U S A. 2003; 100:9138–9143. [PubMed: 12886020]
16. Rosi NL, et al. Oligonucleotide-modified gold nanoparticles for intracellular gene regulation. Science. 2006; 312:1027–1030. [PubMed: 16709779]
17. Jain PK, El-Sayed IH, El-Sayed MA. Au nanopartices target cancer. Nano Today. 2007; 2:18–29.
18. Chithrani BD, Chan WC. Elucidating the mechanism of cellular uptake and removal of protein-coated gold nanoparticles of different sizes and shapes. Nano letters. 2007; 7:1542–1550. [PubMed: 17465586]
19. Kasinskas RW, Forbes NS. Salmonella typhimurium specifically chemotax and proliferate in heterogeneous tumor tissue in vitro. Biotechnol Bioeng. 2006; 94:710–721. [PubMed: 16470601]
20. Kim BJ, Forbes NS. Flux analysis shows that hypoxia-inducible-factor-1-alpha minimally affects intracellular metabolism in tumor spheroids. Biotechnol Bioeng. 2007; 96:1167–1182. [PubMed: 17009333]
21. Freyer JP, Sutherland RM. Selective Dissociation and Characterization of Cells from Different Regions of Multicell Tumor Spheroids. Cancer Res. 1980; 40:3956–3965. [PubMed: 7471046]
22. Kasinskas RW, Forbes NS. Salmonella typhimurium lacking ribose chemoreceptors localize in tumor quiescence and induce apoptosis. Cancer Res. 2007; 67:3201–3209. [PubMed: 17409428]
23. Sutherland RM. Cell and Environment Interactions in Tumor Microregions - the Multicell Spheroid Model. Science. 1988; 240:177–184. [PubMed: 2451290]
24. Kim BJ, Forbes NS. Single-cell analysis demonstrates how nutrient deprivation creates apoptotic and quiescent cell populations in tumor cylindroids. Biotechnol Bioeng. 2008; 101:797–810. [PubMed: 18814293]
25. Helmlinger G, Yuan F, Dellian M, Jain RK. Interstitial pH and pO2 gradients in solid tumors in vivo: high-resolution measurements reveal a lack of correlation. Nat Med. 1997; 3:177–182. [PubMed: 9018236]
26. De M, You CC, Srivastava S, Rotello VM. Biomimetic interactions of proteins with functionalized nanoparticies: A thermodynamic study. J Am Chem Soc. 2007; 129:10747–10753. [PubMed: 17672456]
27. Chompoosor A, Han G, Rotello VM. Charge dependence of ligand release and monolayer stability of gold nanoparticles by biogenic thiols. Bioconjug Chem. 2008; 19:1342–1345. [PubMed: 18553895]
28. Hong R, et al. Glutathione-mediated delivery and release using monolayer protected nanoparticle carriers. J Am Chem Soc. 2006; 128:1078–1079. [PubMed: 16433515]
29. Jones DP, et al. Glutathione measurement in human plasma Evaluation of sample collection, storage and derivatization conditions for analysis of dansyl derivatives by HPLC. Clin Chim Acta. 1998; 275:175–184. [PubMed: 9721075]

30. Hassan SSM, Rechnitz GA. Determination of Glutathione and Glutathione-Reductase with a Silver Sulfide Membrane-Electrode. Anal Chem. 1982; 54:1972–1976.
31. Baldwin AL, Wu NZ, Stein DL. Endothelial Surface-Charge of Intestinal Mucosal Capillaries and Its Modulation by Dextran. Microvasc Res. 1991; 42:160–178. [PubMed: 1719353]
32. Ghitescu L, Fixman A. Surface-Charge Distribution on the Endothelial-Cell of Liver Sinusoids. J Cell Biol. 1984; 99:639–647. [PubMed: 6430915]
33. Chen AM, et al. Oligodeoxynucleotide nanostructure formation in the presence of polypropyleneimine dendrimers and their uptake in breast cancer cells. Nanotechnology. 2006; 17:5449–5460.
34. Holzapfel V, Musyanovych A, Landfester K, Lorenz MR, Mailander V. Preparation of fluorescent carboxyl and amino functionalized polystyrene particles by miniemulsion polymerization as markers for cells. Macromol Chem Phys. 2005; 206:2440–2449.
35. Mislick KA, Baldeschwieler JD. Evidence for the role of proteoglycans in cation-mediated gene transfer. Proc Natl Acad Sci U S A. 1996; 93:12349–12354. [PubMed: 8901584]
36. Tauskela JS, et al. Evaluation of glutathione-sensitive fluorescent dyes in cortical culture. Glia. 2000; 30:329–341. [PubMed: 10797613]
37. Orwar O, Fishman HA, Ziv NE, Scheller RH, Zare RN. Use of 2,3-Naphthalenedicarboxaldehyde Derivatization for Single-Cell Analysis of Glutathione by Capillary Electrophoresis and Histochemical-Localization Ion by Fluorescence Microscopy. Anal Chem. 1995; 67:4261–4268. [PubMed: 8633771]
38. Davies CD, Berk DA, Pluen A, Jain RK. Comparison of IgG diffusion and extracellular matrix composition in rhabdomyosarcomas grown in mice versus in vitro as spheroids reveals the role of host stromal cells. Br J Cancer. 2002; 86:1639–1644. [PubMed: 12085216]
39. Pluen A, et al. Role of tumor-host interactions in interstitial diffusion of macromolecules: Cranial vs. subcutaneous tumors. Proc Natl Acad Sci U S A. 2001; 98:4628–4633. [PubMed: 11274375]
40. Ramanujan S, et al. Diffusion and convection in collagen gels: Implications for transport in the tumor interstitium. Biophys J. 2002; 83:1650–1660. [PubMed: 12202388]
41. Kleinman HK, et al. Isolation and Characterization of Type-Iv Procollagen, Laminin, and Heparan-Sulfate Proteoglycan from the Ehs Sarcoma. Biochemistry (Mosc). 1982; 21:6188–6193.
42. Boucher Y, Baxter LT, Jain RK. Interstitial pressure gradients in tissue-isolated and subcutaneous tumors: implications for therapy. Cancer Res. 1990; 50:4478–4484. [PubMed: 2369726]
43. Jain RK. Transport of molecules in the tumor interstitium: a review. Cancer Res. 1987; 47:3039–3051. [PubMed: 3555767]
44. Young JS, Lumsden CE, Stalker AL. The significance of the tissue pressure of normal testicular and of neoplastic (Brown-Pearce carcinoma) tissue in the rabbit. J Pathol Bacteriol. 1950; 62:313–333. [PubMed: 14784896]
45. You CC, De M, Rotello VM. Contrasting effects of exterior and interior hydrophobic moieties in the complexation of amino acid functionalized gold clusters with alpha-chymotrypsin. Org Lett. 2005; 7:5685–5688. [PubMed: 16321022]
46. Paciotti GF, et al. Colloidal gold: a novel nanoparticle vector for tumor directed drug delivery. Drug delivery. 2004; 11:169–183. [PubMed: 15204636]

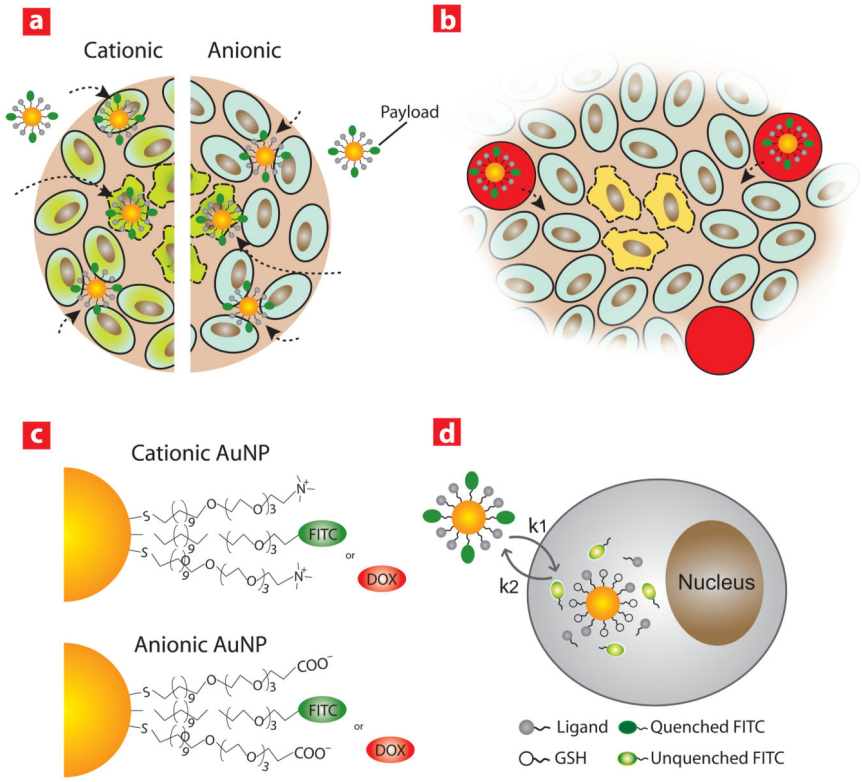

Figure 1. Schematic showing the delivery of payload by gold nanoparticles

a, Delivery of payload (green ovals) into tumour cylindroids by gold nanoparticles (gold circles). Cells containing released FITC-SH are in green. Viable cells are shown with smooth, solid boundaries, whereas necrotic cells have rough, dashed boundaries. Dotted arrowhead lines indicate diffusion and cellular uptake. In cylindroids, nanoparticles are present in the medium outside the boundary of the cell mass. b, Intratumoral delivery by gold nanoparticles following extravasation from the vessel lumen (red circles). c, Mixed monolayer-protected gold nanoparticles loaded with thioalkylated FITC or doxorubicin (DOX). d, Cellular uptake and FITC-SH release by thiol-mediated replacement reactions.

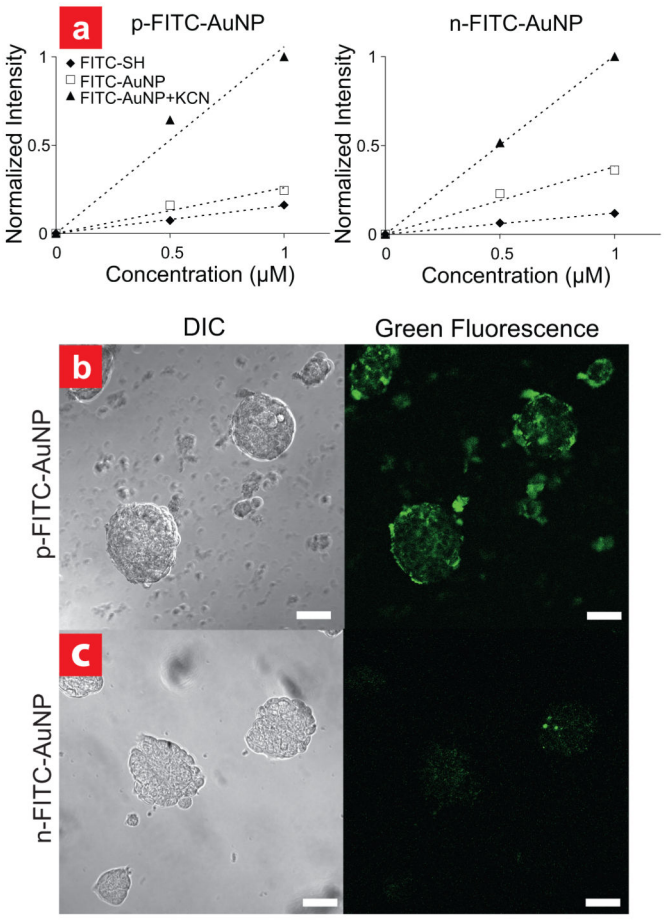

Figure 2. Fluorescence calibration and cellular uptake/release of FITC-AuNPs

a, Normalized fluorescence intensities plotted against nanoparticle concentration. Dotted lines represent linear least square fitting results. For all components, fluorescence intensity was linearly proportional to concentration. b and c, Differential interference contrast (DIC) and confocal green fluorescent images of cells in monolayer culture incubated with cationic (b) and anionic (c) gold nanoparticles.

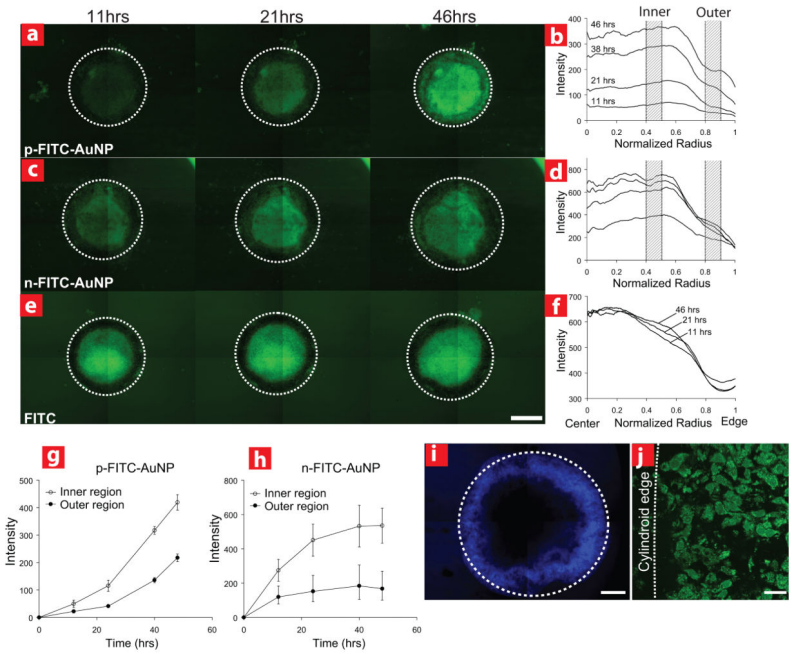

Figure 3. Release of FITC-SH from Au-NPs in tumour cylindroids

a–f, Green fluorescence images and corresponding intensity profiles of cylindroids treated with nanoparticles. Fluorescence images were acquired after incubation with p-FITC-AuNP (a), n-FITC-AuNP (c) and FITC (e) for 11, 21, and 46hrs. Dotted circles indicate cylindroid edges and scale bar is 300mm. In b and d, fluorescence intensity profiles are shown at 11, 21, 38, and 46hrs. g and h, Change of average fluorescence intensities over time in the inner and outer regions of cylindroids (indicated with hashed bars in panel b and d) after incubation with p-FITC-AuNP (g) and n-FITC-AuNP (h). Errors are standard error of the mean (n=3). i, Blue fluorescence image of a cylindroid incubated with OPA for 18hrs. Scale bar is 200μm. j, green confocal fluorescence microscope image of the outer region of the cylindroid treated with p-FITC-AuNP. Scale bar is 20mm.

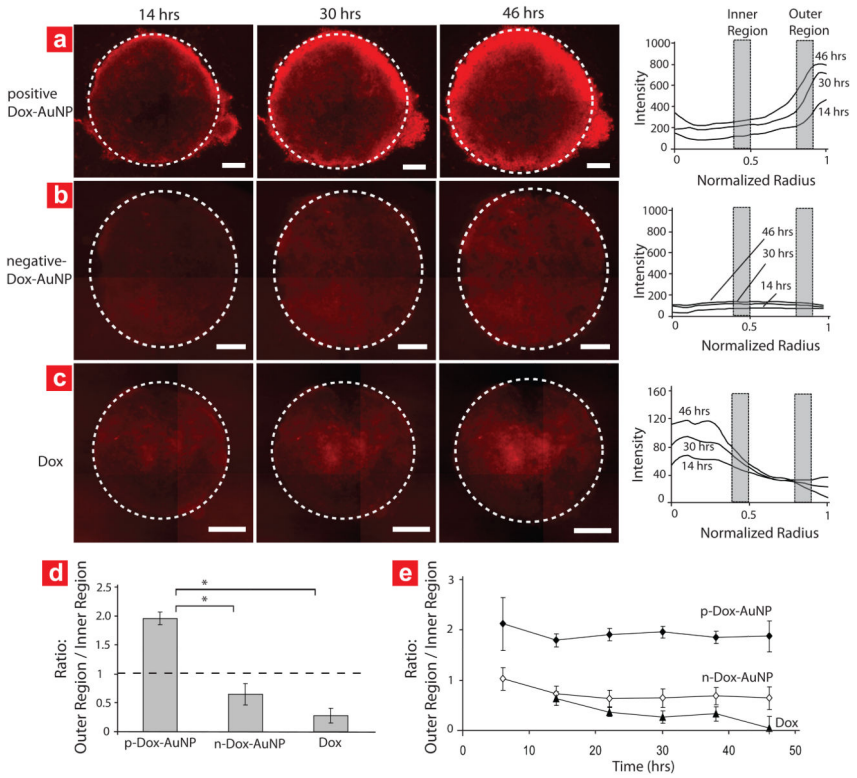

Figure 4. Doxorubicin release in cylindroids

a–c, Red fluorescence images and the corresponding radial intensity profiles of cylindroids treated with positive Dox-AuNP (a), negative Dox-AuNP (b) and free Dox (c). Dotted circles indicate cylindroid edges. Scale bars are 200μm. d and e, Ratio of average fluorescence intensities in the outer region to those in the inner region of cylindroids, 30 hours after treatment (d) and as a function of time (e). Errors are standard error of the mean, and significance was determine using Student's t-test (*, $P<0.05$; n=3).

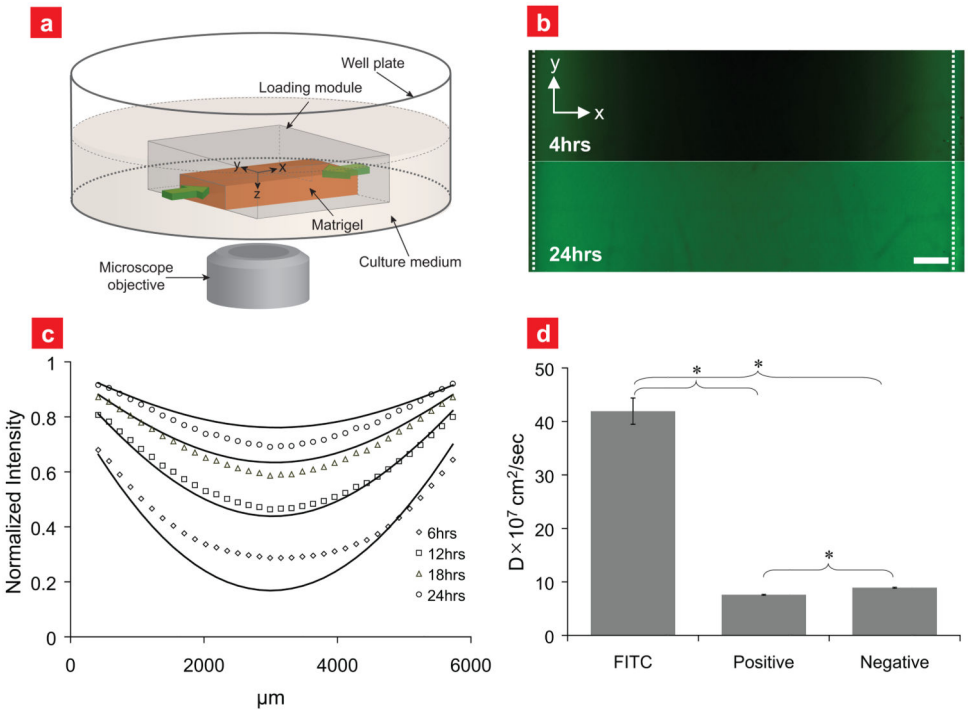

Figure 5. Effect of surface charge on diffusivity through extracellular matrix material

a, Schematic representation of loading module filled with Matrigel. **b**, Green fluorescence images acquired from the bottom of the loading module 4 and 24hrs after adding particles. Dotted lines at both ends indicate Matrigel edges. Scale bar is 500μm. **c**, Fluorescence intensity profiles in Matrigel along the x-axis as a function of time (symbol) and intensity profiles generated by fitting to a Fickian diffusion model (solid lines). **d**, Comparison of diffusion coefficients of FITC, cationic and anionic gold nanoparticles in Matrigel (*, $P<0.005$; n=3).

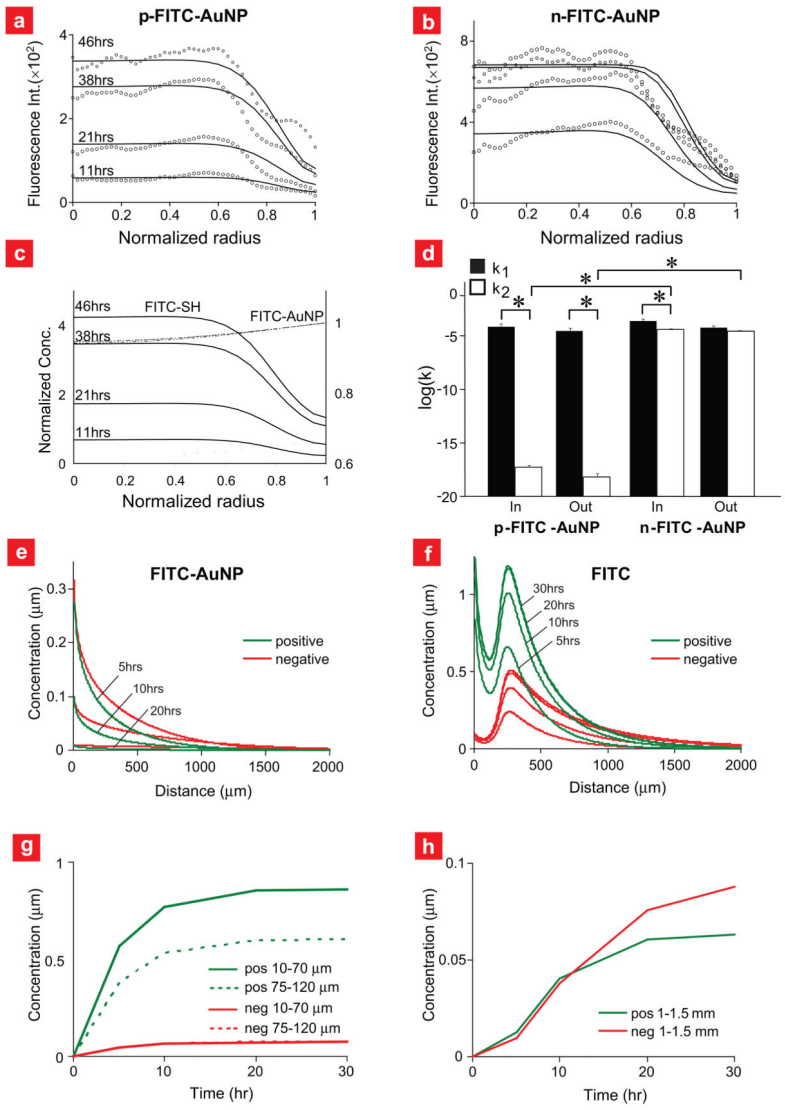

Figure 6. Rate constants of cellular uptake and predictions of particle and ligand distribution in tumours

a and b, Fluorescence intensity profiles measured in fluorescence images of cylindroids (symbol) and those predicted by the mathematical model (solid lines). Concentrations were normalized by the maximum concentration of FITC-AuNP in cylindroids. **c,** Independent concentration profiles of fluorophore bound to nanoparticles (FITC-AuNP) and released fluorophore ligand (FITC-SH) predicted by the computation model. **d,** Comparison of forward (k_1) and reverse (k_2) rate constants between different regions. Errors are standard error of the mean, and significance was determine using Student's t-test (*, $P<0.05$). **e** and **f,** Modeled concentrations of FITC-AuNPs and released FITC-SH as a function of distance from blood vessels of a hypothetical tumour. Clearance half-life of FITC-AuNPs was assumed to be 3hrs. **g,** Average concentrations of FITC-AuNPs in the region between 10–70 μm (proliferating) and 75–120 μm (quiescent) from the blood vessel wall as a function of

time. **h**, Average concentrations of released FITC in deep tumour regions (1.0–1.5 mm) as a function of time.